





## Accelerating the prediction of stacking fault energy by combining *ab initio* calculations and machine learning

Albert Linda <sup>1</sup>, Md. Faiz Akhtar <sup>1</sup>, Shaswat Pathak <sup>2</sup>, and Somnath Bhowmick <sup>1,\*</sup>

<sup>1</sup>*Department of Materials Science and Engineering, Indian Institute of Technology Kanpur, Kanpur 208016, India*

<sup>2</sup>*Department of Mechanical Engineering, SRM College of Engineering and Technology, Kattankulathur-Chennai 603203, India*



(Received 22 March 2024; revised 12 May 2024; accepted 15 May 2024; published 3 June 2024)

Stacking fault energies (SFEs) are key parameters to understand the deformation mechanisms in metals and alloys, and prior knowledge of SFEs from *ab initio* calculations is crucial for alloy design. Machine learning (ML) algorithms used in the present work show a  $\sim 80$  times acceleration of generalized stacking fault energy predictions, which are otherwise computationally very expensive to get directly from density functional theory calculations, particularly for alloys. The origin of the features used for training the ML algorithms lies in the physics-based Friedel model, and the present work uncovers the connection between the physics of *d* electrons and the deformation behavior of transition metals and alloys. Predictions based on the ML model agree with the experimental data. Our model can be helpful in accelerated alloy design by providing a fast method of screening materials in terms of stacking fault energies.

DOI: [10.1103/PhysRevB.109.214102](https://doi.org/10.1103/PhysRevB.109.214102)

### I. INTRODUCTION

Stacking fault (SF) in face-centered-cubic (fcc) materials is a planar defect that arises during plastic deformation through dissociating a perfect dislocation into two Shockley partial dislocations. Stacking fault energy (SFE) is a crucial parameter that determines the deformation mechanisms of fcc materials. Materials with low-to-medium SFE generally deform via transformation-induced plasticity (TRIP) or twinning-induced plasticity (TWIP), while those with high SFE deform via dislocation slip. SFE depends on several parameters such as temperature [1,2] and stress [3,4] and it can be tuned via alloying [5–8]. Since SFE dictates dislocation dissociation, it is one of the determining factors for the dislocation pile-up at the twin boundaries (TBs), resulting in fatigue cracking [9]. Deformation processing (such as ball milling, rolling, and torsion) or lattice mismatch-induced interface strain can form high-density SFs in low-to-medium SFE metals, leading to strain hardening while maintaining good ductility [10]. SFE plays a major role in the mechanical properties of bulk nanostructured materials processed via severe plastic deformation [11]. The creep life of Ni-based superalloys improves due to SFE reduction by alloying with Co [12]. Due to its importance in the mechanical behavior of metals, several experimental and computational methods have been developed for SFE estimation, as discussed below.

Experimentally, SFEs are estimated by transmission electron microscopy (TEM) or by x-ray diffraction (XRD) and neutron diffraction (ND). Using TEM, the intrinsic SFE is estimated by measuring the stacking fault width, which is defined as the separation distance of isolated pairs of leading and trailing partial dislocations. This method assumes a balance

between the excess energy stored in the stacking fault and the elastic strain energy responsible for the mutual repulsion of leading and trailing partials [13]. The determination of SFE through XRD and ND involves analyzing the shift and broadening of the Bragg peak, considering the relationship between stacking fault probability, dislocation density, and intrinsic SFE [14]. An *in situ* XRD method to measure the critical stress in the early stage of plastic deformation provides another way to estimate SFE experimentally [15,16].

The experimental methods mentioned above have one limitation—SFE at any unstable point (lying between perfect and faulted crystal) cannot be estimated. Such curves with SFE values at multiple points between perfect and faulted crystals are known as the generalized stacking fault energy (GSFE) profile or  $\gamma$  surface. Computational methods such as density functional theory (DFT) or classical molecular dynamics (MD) are used to calculate the  $\gamma$  surface [4,17–21]. The  $\gamma$  surface represents the potential energy landscape between adjacent planes in a slip system. The simulated  $\gamma$  surface acts as an input for calculating the Peierls stresses via the Peierls-Nabarro model (P-N model) for studying dislocations [22–30], plastic deformation in high-entropy alloys [31,32], and phase transitions [33,34]. Due to its *ab initio* nature, the  $\gamma$  surface predicted by DFT is believed to be very accurate, and the SFE values are in reasonable agreement with experimental findings. However, the DFT calculation predicts negative SFEs for some materials such as metastable alloys, which are experimentally reported to have small but positive SFE [35–41]. Several attempts have been made to understand the reasons behind the discrepancy, further establishing the reliability of DFT for SFE prediction [14,42].

The accuracy and reliability of DFT for SFE prediction lies in its ability to accurately incorporate the effect of electronic contributions [43–49]. For example, Harris *et al.* showed the connection between the electronic structure (empty *d* states)

\*bsomnath@iitk.ac.in

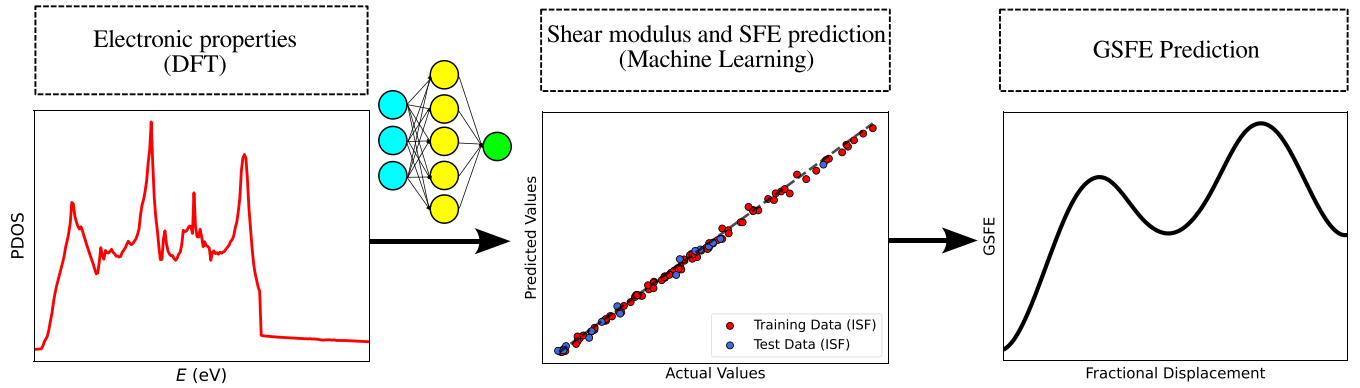


FIG. 1. Workflow for physics-based accelerated generalized stacking fault energy (GSFE) calculation: *ab initio* electronic density of states (DOS) calculation, followed by machine learning based prediction of stacking fault energy and GSFE curve.

and SFE [50]. Datta *et al.* found that the electronic density of states (DOS) plots for the faulted structures are considerably smoother compared to the pristine materials [51]. A study of the influence of solute substitutions in Ni on its GSFE found a correlation between density of state (DOS) and intrinsic stacking fault (ISF) energy [52]. The energy barriers for both deformation slip and twinning formation decrease with the increased electron concentrations in ZnS, ZnTe, and CdTe [53]. A recent study also revealed a direct correlation of SFE with the width of the *d* band of fcc transition metals [4]. As suggested by the previous studies, a deep connection exists between the electronic band structure and SFE, which we would like to explore in detail in the present work.

In contemporary times, machine learning (ML) algorithms have emerged as practical tools capable of achieving robust predictive outcomes for a given input dataset. Recent reports highlight the application of ML in several domains of materials science and engineering, such as potential development [54], microstructure modeling [55], and structure-property correlation [56,57]. In alloy development, ML has been employed to predict phase stability, glass forming ability, and properties as a function of alloy composition [58–60]. Stacking fault energy, the subject matter of this paper, has also been predicted using ML models using local composition, atomic size, electronic structure, and physical, thermomechanical, and elastic properties as descriptors [61–66]. However, it is noteworthy that the values of these fundamental properties for alloys are often estimated using the rule of mixture, introducing potential discrepancies in the results. A few studies have attempted to predict SFE using the charge density obtained from DFT calculations [67,68].

The focus of the present work lies in its use of the physics-based Friedel model to derive the features for machine learning. The physics-based model helps us to uncover the connection between the SFE and electronic band structure of fcc transition metals and alloys. A schematic diagram is illustrated in Fig. 1. First, we calculate the electronic density of states (DOS), a routine job for DFT packages. Using the electronic DOS data, we calculate some parameters such as the width of the *d* band ( $W_d$ ), energy at the band center ( $\epsilon_d$ ), electrons in the *d* orbital ( $z_d$ ), and electrons in the *s* orbital ( $z_s$ ). Using various machine learning models [Gaussian process regression (GPR), support vector regression (SVR), deep neural

network (DNN), and random forest], we are able to predict the stacking fault energy and shear modulus of transition metals and alloys using the parameters obtained from DOS. Values predicted by the ML models agree with the experimental data. We are also able to predict the GSFE curve with reasonable accuracy, and our combined *ab initio*–ML approach can accelerate the GSFE calculation 80x faster compared to the solely *ab initio* based approach in the case of alloys. Our work paves the way for fast and accurate computational prediction of transition metal alloys with desired SFE values, providing a valuable understanding of the deformation mechanism and mechanical behavior.

## II. METHODOLOGY

Density functional theory (DFT) calculations, as implemented in the Vienna *ab initio* Simulation Package (VASP) [69], are performed using a plane-wave basis set (with a 400 eV kinetic energy cutoff) and projector augmented wave (PAW) potentials [70]. The generalized gradient approximation (GGA), applying Perdew, Burke, and Ernzerhof (PBE) as the exchange-correlation functional [71], is used. The unit cell parameters and atomic coordinates are fully relaxed until the energy converges to within  $10^{-6}$  eV and the atomic force dips below  $0.01$  eV/Å. Further details about the supercell size and *k*-point mesh used for Brillouin zone sampling are given in the respective sections.

## III. RESULTS AND DISCUSSION

### A. Stacking fault energy calculations

#### 1. SFE using periodic supercell

We consider an ideal fcc structure composed of nine layers stacked in an  $\dots ABCABCABC \dots$  pattern [Fig. 2(a)]. Two of the cell vectors,  $\frac{1}{2}[\bar{1}10]$  and  $\frac{1}{2}[\bar{1}01]$ , lie on the (111) plane, while the third one is perpendicular to the (111) plane and aligned along the [111] direction. An intrinsic stacking fault (ISF) has a stacking sequence of  $\dots ABCABABCABC \dots$ , as shown in Fig. 2(a).

An ISF is created by fixing the bottom five layers and displacing each of the top four layers by the Burgers vector  $\vec{b} = \frac{1}{6}[\bar{2}11]$ . Simultaneously, we shift the out-of-plane cell

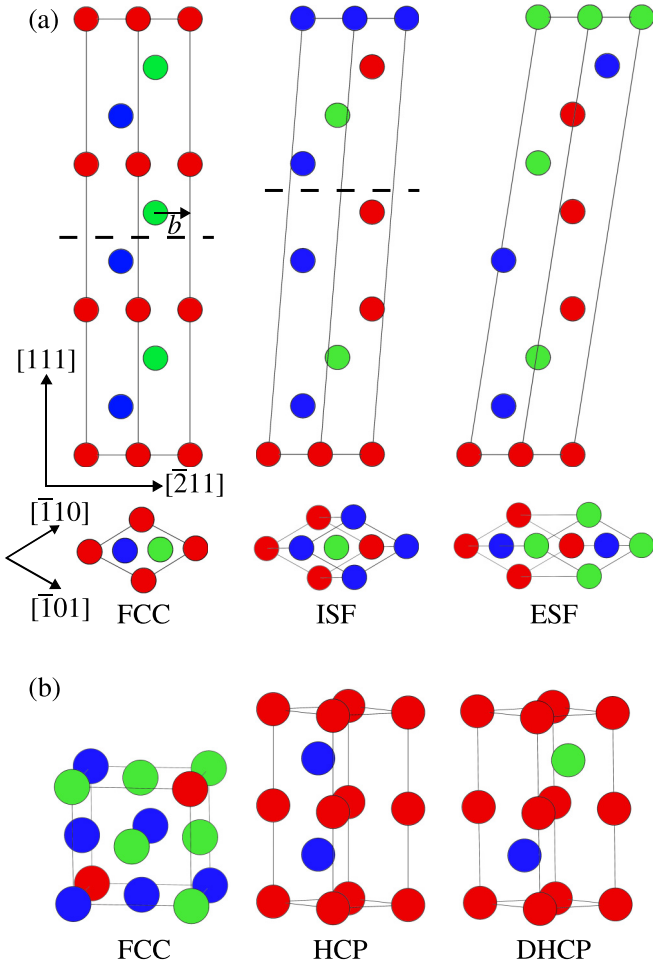


FIG. 2. (a) Supercell method: side view (first row) and top view (second row) of the supercell of the face centered cubic (fcc) (left), intrinsic stacking fault or ISF (center), and extrinsic stacking fault or ESF (right). Starting from the fcc structure, all the atoms located above the dotted line and the out-of-plane cell vector are displaced by  $\vec{b}$  ( $2\vec{b}$ ) to go from the fcc to ISF (ESF) structure. (b) ANNNI model: fcc, hexagonal closed packed (hcp), and double hexagonal closed packed (dhcp) cells used for the stacking fault energy calculations. In both (a) and (b), the A, B, and C stacking sequence of atoms along the closed packed direction is represented in red, blue, and green colors, respectively.

vector (initially oriented along the  $[111]$  direction) by the same vector  $\vec{b}$  to preserve the unit cell's periodicity. This approach enables us to compute the stacking fault energy using periodic cells, eliminating the need to introduce surface layers [76]. We define the intrinsic stacking fault energy  $\gamma_{\text{ISF}}$  as the energy difference between the faulted and ideal structures per unit area,

$$\gamma_{\text{ISF}} = \frac{E_{\text{ISF}} - E_{\text{fcc}}}{A}. \quad (1)$$

To get the energy values for metals from DFT calculations, we use a  $21 \times 21 \times 2$   $k$ -point mesh.

An extrinsic stacking fault (ESF) has a stacking sequence of  $\dots ABCABACABC \dots$ , as shown in Fig. 2(a). Starting with the ISF structure, we now fix the bottom six layers and

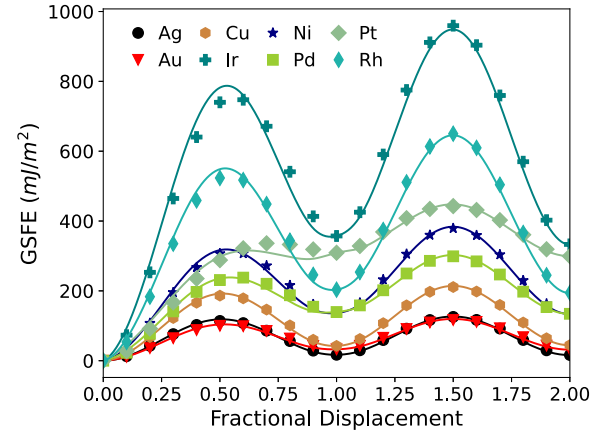


FIG. 3. Generalized stacking fault energy (GSFE) curves for fcc metals, illustrated along the  $[\bar{2}11]$  direction. Energy values are plotted from 0 to  $2\vec{b}$ , where Burgers vector  $\vec{b} = \frac{1}{6}[\bar{2}11]$ . Symbols depict DFT values, while the curves are fitted using Eq. (2).

displace the top three layers by  $\vec{b} = \frac{1}{6}[\bar{2}11]$ . The out-of-plane cell vector is also shifted by  $\vec{b}$ , yielding the ESF stacking sequence [Fig. 2(a)]. Notably, in the case of ESF, the top three layers and the out-of-plane cell vector are displaced by  $2\vec{b}$  relative to the ideal fcc configuration. To determine the  $\gamma_{\text{ESF}}$  value, we employ an expression similar to Eq. (1).

Apart from the  $\gamma_{\text{ISF}}$  and  $\gamma_{\text{ESF}}$ , we compute stacking fault energies at various displacements, ranging from 0 to  $2\vec{b}$ , with a step size of  $0.1\vec{b}$  to delineate the entire GSFE curve, as shown in Fig. 3. Two significant peaks along the GSFE curve are noteworthy: one situated at approximately the middle of the ideal fcc and ISF [referred to as the unstable stacking fault (USF)] and the other located at approximately the middle of ISF and ESF [referred to as the unstable twinning fault (UTF)]. These peaks represent the energy barriers for forming ISF and ESF, respectively.

We illustrate the GSFE curves of all the transition and noble metals having a fcc ground state in Fig. 3. The symbols in the figure represent the values calculated from DFT. The curves are drawn using the following expressions:

$$\gamma = \begin{cases} cG \sin^2(\pi x) + \gamma_{\text{ISF}}x, & 0 \leq x \leq 1 \\ cG \sin^2(\pi x) + \gamma_{\text{ISF}}(2-x) + \gamma_{\text{ESF}}(x-1), & 1 \leq x \leq 2, \end{cases} \quad (2)$$

where  $\gamma_{\text{ISF}}$ ,  $\gamma_{\text{ESF}}$ , and shear modulus  $G$  are calculated from DFT,  $c$  is a constant, and  $x$  is the fractional displacement in terms of Burgers vector  $\vec{b}$ . The values of  $c$  are 5.01 for Ag, 5.67 for Au, 3.43 for Cu, 3.74 for Pd, 2.96 for Pt, 2.61 for Ni, 3.04 for Rh, and 2.81 for Ir. We calculate the shear modulus via the strain-energy approach [77] by using the VASPKIT tool [78], details of which are given in Sec. I of the Supplemental Material (SM) [79]. In conclusion, one can generate the entire GSFE curve with reasonable accuracy by calculating three numbers, i.e.,  $\gamma_{\text{ISF}}$ ,  $\gamma_{\text{ESF}}$ , and  $G$ , from DFT. Such an approach is computationally cheaper than calculating the entire GSFE curve from DFT, particularly when dealing with alloys.

TABLE I. Comparison of SFEs obtained from DFT using two approaches (supercell and ANNNI model), predicted SFEs (using deep neural network or DNN), and experimental data in Refs. [72]<sup>a</sup>, [73]<sup>b</sup>, and [74]<sup>c</sup>. A similar comparison for shear modulus values obtained through DFT, predicted using DNN and experimental values [75]<sup>d</sup>. Both DFT and ML-predicted values are in good agreement with the experimental values. Note that experimental values are indirect measurements using XRD and TEM at room temperature, while the DFT calculations are carried out at 0 K.

Metals	DFT				$G$	Predicted			Expt.	
	Supercell		ANNNI			$\gamma_{\text{ISF}}$	$\gamma_{\text{ESF}}$	$G$	$\gamma_{\text{ISF}}$	$G^d$
	$\gamma_{\text{ISF}}$	$\gamma_{\text{ESF}}$	$\gamma_{\text{ISF}}$	$\gamma_{\text{ESF}}$						
Ag	16.9	16.3	17.5	18.4	22.0	18.1	23.2	22.8	25.0 <sup>a</sup>	27.0
Au	32.6	31.7	23.6	23.3	15.4	32.8	37.5	19.2	45.0 <sup>a</sup>	27.7
Cu	42.4	44.6	48.7	53.3	49.8	43.8	56.3	39.6	55.0 <sup>b</sup>	48.3
Ir	357.2	333.1	348.3	334.3	214.4	359.6	400.3	216.1	480.0 <sup>c</sup>	210.0
Ni	136.6	133.9	140.8	135.0	95.1	138.5	162.7	95.1	125.0 <sup>c</sup>	75.0
Pd	139.5	134.3	146.6	139.5	44.4	137.1	148.3	45.1	130.0 <sup>a</sup>	43.6
Pt	309.1	299.5	277.0	282.6	48.6	299.8	315.6	50.6	322.0 <sup>c</sup>	61.0
Rh	203.4	194.3	190.2	188.2	146.8	207.0	240.4	150.5	330.0 <sup>a</sup>	150.0
Pd-Pt	190.8	180.9	176.0	172.0	45.8	172.2	186.5	47.0		
Ir-Pt	359.5	342.9	328.5	326.2	163.5	326.6	371.5	150.5		
Pd-Au	131.4	128.2	118.0	112.0	37.4	116.0	123.9	37.5		

## 2. SFE using ANNNI model

The axial-next-nearest-neighbor Ising (ANNNI) model is an alternate route to find SFEs. Although the model is computationally less expensive, one can only get the ISF and ESF values instead of the entire GSFE curve. The ANNNI model uses specific combinations of energies corresponding to different short-period stacking sequences of close-packed (111) planes. For example, the second-order approximation to obtain the ISF and ESF energies is given by the following combinations:

$$\begin{aligned} E_{\text{ISF}} &= \frac{E_{\text{hcp}} + 2E_{\text{dhcp}} - 3E_{\text{fcc}}}{A}, \\ E_{\text{ESF}} &= \frac{4(E_{\text{dhcp}} - E_{\text{fcc}})}{A}. \end{aligned} \quad (3)$$

In the above equations,  $A = \frac{\sqrt{3}}{4}a^2$ , where  $a$  is the lattice parameter of a conventional fcc unit cell. Energies of the face-centered-cubic ( $ABCABC$  stacking), hexagonal close-packed ( $ABAB$  stacking), and double hexagonal close-packed ( $ABCACABAC$  stacking) structures are denoted by  $E_{\text{fcc}}$ ,  $E_{\text{hcp}}$ , and  $E_{\text{dhcp}}$ , respectively. The fcc, hcp, and dhcp unit cells used for the SFE calculation using the ANNNI model are illustrated in Fig. 2(b). To get the energy values for metals from DFT calculations, we use  $12 \times 12 \times 12$ ,  $21 \times 21 \times 5$ , and  $21 \times 21 \times 5$   $k$ -point mesh for fcc, hcp, and dhcp, respectively. SFE values calculated from the supercell method and ANNNI model are compared in Table I. Besides Au, values obtained from both models are in remarkable agreement. Note that the ANNNI model used in this work is a second-order approximation. One can further improve the accuracy by using a higher-order approximation [80]. Using machine learning tools such as Gaussian process regression, one may also do a thorough uncertainty analysis, which is beyond the scope of this work.

## B. Friedel model

An understanding of the electronic structure is the primary building block for a comprehensive study of a material's properties. Electrons serve as the quantum glue that keeps the nuclei of a solid together and influences the mechanical, electrical, optical, and magnetic properties of materials. It is well known that  $d$  electrons play a significant role in transition metals' electronic and magnetic properties. Figures 4(a) and 4(b) illustrate the DOS of the  $s$  electrons and  $d$  electrons of Ag and Ir, respectively. Unlike the DOS of  $s$  states, the DOS of  $d$  states is sharply peaked, which indicates that  $d$  states are relatively localized compared to the  $s$  states. Although the DOS curves are quite intricate, Friedel proposed a significant simplification. The DOS of  $s$  states, denoted by  $g_s(\epsilon)$ , is approximated to be free-electron like, obeying  $g_s(\epsilon) \propto \sqrt{\epsilon}$  [Fig. 4(c)]. The DOS of  $d$  states, denoted by  $g_d(\epsilon)$ , is approximated to be a step function [Fig. 4(c)], expressed as

$$\begin{aligned} g_d(\epsilon) &= \frac{10}{W_d}, \quad \epsilon_d - \frac{W_d}{2} < \epsilon < \epsilon_d + \frac{W_d}{2}, \\ &= 0 \quad \text{otherwise.} \end{aligned} \quad (4)$$

The center of the  $d$  band and its width are denoted by  $\epsilon_d$  and  $W_d$ , which are related to the projected density of states (PDOS) of the  $d$  band. The first moment of the DOS with respect to the Fermi energy ( $\epsilon_F$ ) is

$$\mu = \int (\epsilon - \epsilon_F) g_d^{\text{DFT}}(\epsilon) d\epsilon, \quad (5)$$

where  $g_d^{\text{DFT}}(\epsilon)$  is the PDOS of the  $d$  band, obtained from the *ab initio* calculations. The number  $\epsilon_d = (\epsilon_F - |\mu|)$  corresponds to the center of the  $d$  band. Further, we calculate the second moment of the DOS with respect to  $\epsilon_d$ ,

$$\sigma^2 = \int (\epsilon - \epsilon_d)^2 g_d^{\text{DFT}}(\epsilon) d\epsilon. \quad (6)$$

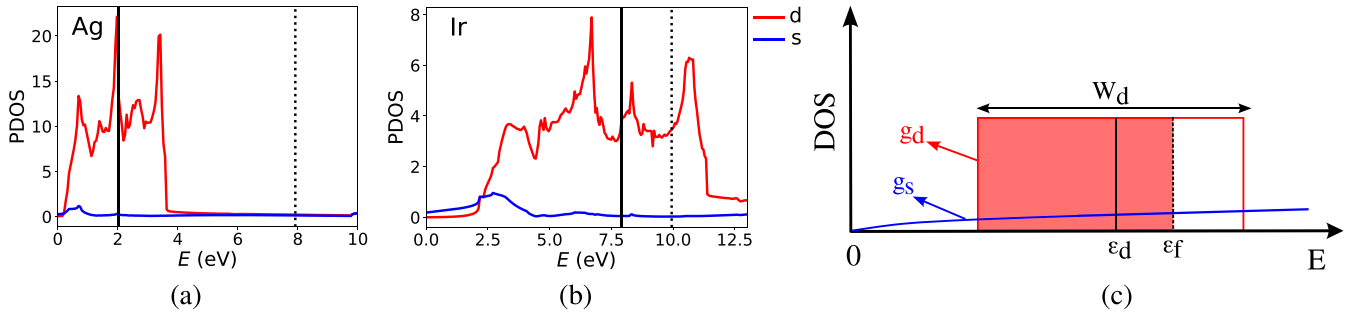


FIG. 4. Orbital projected density of states for (a) Ag (completely full narrow  $d$  band, low SFE) and (b) Ir (partially full wide  $d$  band, high SFE). The black solid line denotes the  $d$ -band center ( $\epsilon_d$ ), while the dotted line represents the Fermi energy ( $E_F$ ). (c) Schematic  $s$ -band and  $d$ -band electronic density of states, according to the Friedel model.

We define the width of the  $d$  band as  $W_d = 2\sigma$ . As shown in Figs. S1 and S2 in the SM [79], the periodic trend of the calculated  $\epsilon_d$  and  $W_d$  agrees with the solid-state table [81].

It is evident that unlike  $s$  states,  $d$  states cannot be treated using free-electron theory, and a tight-binding-like description would be more appropriate. In a tight-binding description, the bandwidth is an important parameter that depends on the overlap of atomic orbitals. For example, core states have zero width because of no overlap. Valence  $d$  states have a finite width, leading to some energy gain, depending on  $W_d$ . Using the DOS expression in Eq. (4), one can illustrate that the energy gain is

$$E_d = 5W_d \left[ -\frac{z_d}{10} + \left( \frac{z_d}{10} \right)^2 \right], \quad (7)$$

where  $z_d$  is the number of electrons in the  $d$  band. We compute  $z_d$  from the *ab initio* calculations by integrating the  $d$ -band PDOS up to the Fermi energy. We obtain  $W_d$  from *ab initio* calculations using Eq. (6). We define  $E_d$  as the cohesive energy due to the overlap of adjacent  $d$  bands. The term within the square bracket in Eq. (7) has a minimum at  $z_d = 5$  (middle of the transition metal series), and it is zero at  $z_d = 10$  (noble metal). Our *ab initio* calculations confirm that  $z_d$  increases as we move from left to right of a row in the periodic table (Fig. S3 in the SM [79]). However,  $z_d$  is slightly less than 10 in noble metals, as some electrons are transferred to the free-electron-like band. Interestingly, we also find a periodic trend in  $W_d$  along a particular row; values increase from the left to the center and decrease from the center to the noble metal. In other words,  $W_d$  has a maximum near the middle of the transition metal series (Fig. S2 in the SM [79]). According to the Friedel model, the binding energy [Eq. (7)] of transition metals is maximum near the middle of a row (Fig. S4 in the SM [79]). This trend is in reasonably good agreement with experimental values. For example, the melting point is higher near the middle of the transition metal series (Fig. S4 in the SM [79]). Such a correlation makes the Friedel model credible despite its simplicity.

We calculate the Wigner-Seitz radius  $r_0$  by equating the volume per atom (obtained from *ab initio*) to  $4\pi r_0^3/3$ . Values of  $r_0$  obtained from *ab initio* agree well with the ones reported in the solid-state table (Fig. S5 in the SM [79]). Since  $d$ -band overlap decreases with increasing distance between the atoms, we assume bandwidth  $W_d \propto r_0^{-\alpha}$ . As a result, the volume

dependence of  $E_d$ , denoted by  $\kappa_d$ , can be expressed as

$$\kappa_d = \frac{\partial E_d}{\partial r_0} = \frac{5\alpha W_d}{r_0} \left[ \frac{z_d}{10} - \left( \frac{z_d}{10} \right)^2 \right]. \quad (8)$$

Similar to  $E_d$ ,  $\kappa_d$  also peaks near the middle of the transition metal series (Fig. S6 in the SM [79]).

In summary, the Friedel model defines binding among  $d$  electrons in terms of specific material parameters, which can be computed from the electronic density of states obtained from *ab initio* calculations. In the following section, we use these parameters to fit a machine learning model, which can predict SFE values of transition metals and binary alloys.

## C. Machine learning

### 1. Data generation using ANNNI model

We use the ANNNI model to generate an extensive database of  $\gamma_{\text{ISF}}$  and  $\gamma_{\text{ESF}}$  values for Au-Pd, Pd-Ag, Ag-Au, Rh-Pd, Ir-Pd, Pd-Pt, Cu-Pt, Ir-Pt, Ni-Ag, Ni-Au, Ni-Pd, Ni-Pt, Ni-Rh, and Ni-Cu binary alloys. These alloys are

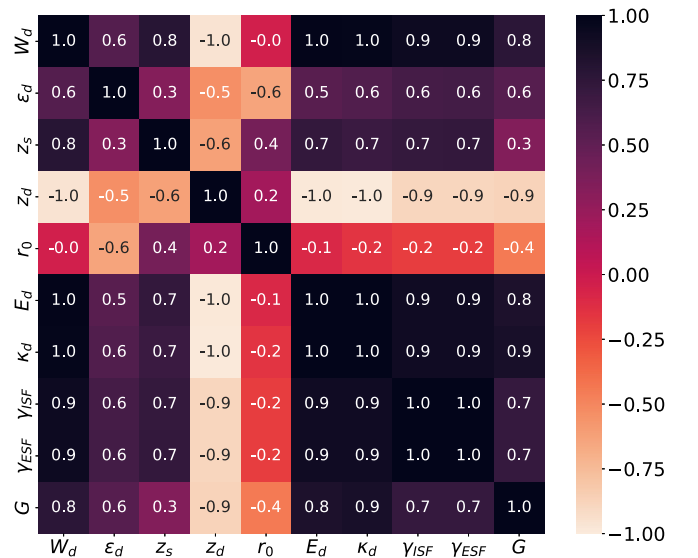


FIG. 5. Heat map of Pearson correlation coefficient matrix: target variables are  $\gamma_{\text{ISF}}$ ,  $\gamma_{\text{ESF}}$ ,  $G$  and feature variables are  $W_d$ ,  $\epsilon_d$ ,  $z_s$ ,  $z_d$ ,  $r_0$ ,  $E_d$ ,  $\kappa_d$ . Values close to black (white) indicate strongly positive (negative) correlations.

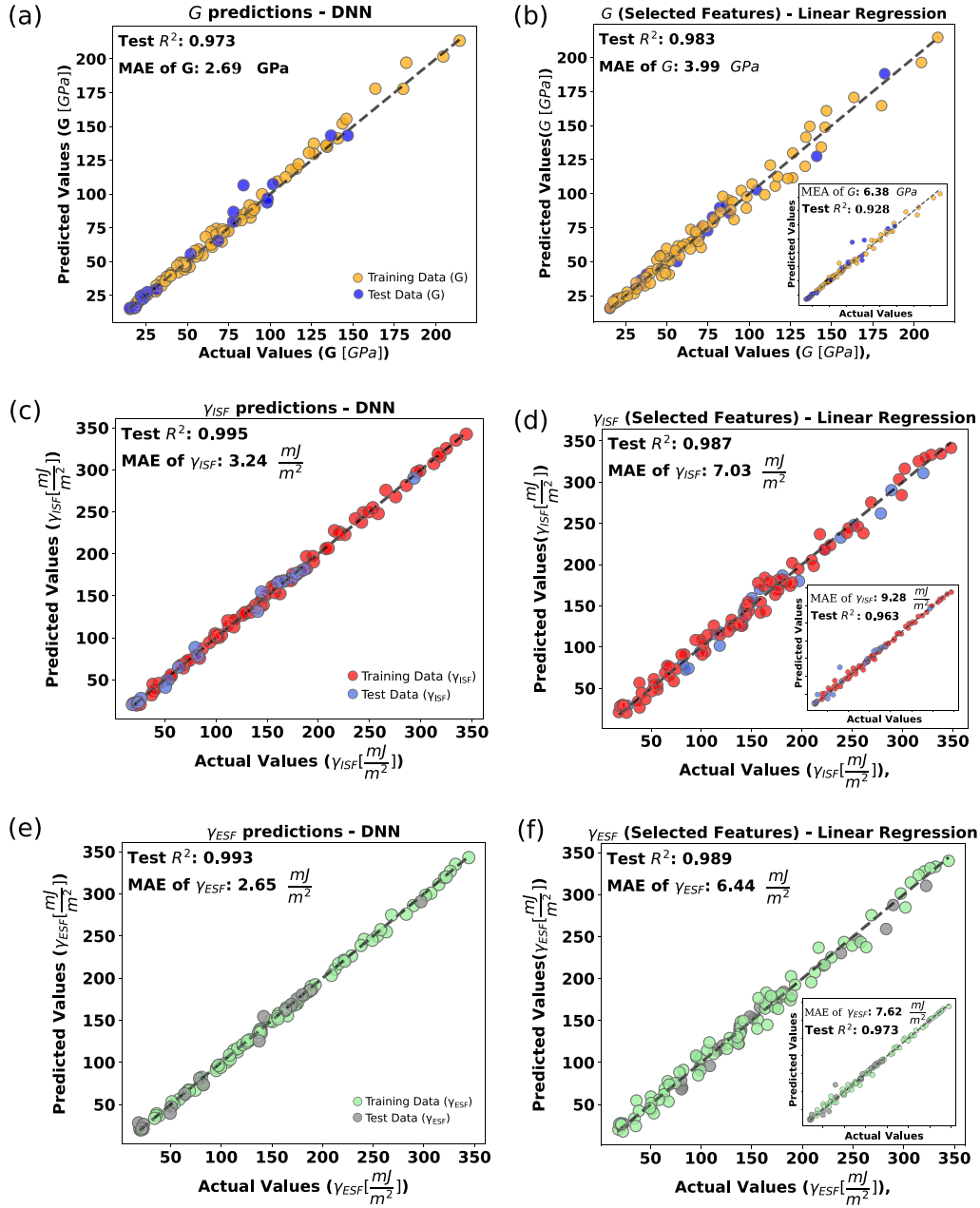


FIG. 6. (a),(c),(e) Comparison between actual and predicted values from DNNs for  $G$ ,  $\gamma_{ISF}$ , and  $\gamma_{ESF}$ , respectively. (b),(d),(f) The same for selected features using Eqs. (9), (10), and (11), while the insets illustrate the outcomes of random forest regression with all of the features.

selected because of the solid solubility of the two elements throughout the composition range, spanning from 12.5% to 87.5%, with intervals of 12.5%, encompassing seven compositions for each alloy. Using the ATAT package [82], we generate special quasirandom structures (SQS) to describe the random arrangement of constituent atoms in a binary alloy. We generate three types of supercells, each containing 32 atoms: a conventional  $2 \times 2 \times 2$  fcc supercell, a  $2 \times 2 \times 4$  hcp supercell, and a  $2 \times 2 \times 2$  dhcp supercell. We use a  $k$ -point mesh of  $12 \times 12 \times 12$  for fcc, and  $21 \times 21 \times 5$  for hcp and dhcp supercells. The complete dataset for training and testing the ML model contains  $\gamma_{ISF}$ ,  $\gamma_{ESF}$ , and  $G$  values for eight metals and all the binary alloys

mentioned above. We also calculate the  $d$ -band PDOS and related parameters [Fig. 4(c)] using the fcc supercell of the metals and alloys.

## 2. Feature and model selection

We aim to train a model to predict  $\gamma_{ISF}$ ,  $\gamma_{ESF}$ , and  $G$  of a material from its DOS, such that one can generate the GSFE curves using Eq. (2). For the purpose of prediction, we use  $\varepsilon_d$ ,  $W_d$ ,  $z_d$ ,  $r_0$ , and  $z_s$  (number of  $s$  electrons) as feature variables. Except  $r_0$ , the rest of the features have moderate to high values of correlation coefficients (Fig. 5). Notably,  $z_d$  (number of  $d$  electrons) has a very high negative correlation with

SFEs, which implies lower SFE for a material with higher  $z_d$ . This observation agrees with the experimental facts that noble metals (Au, Ag, Cu) have low SFEs, as they have the highest  $d$  electrons. Bandwidth  $W_d$  has a very high positive correlation with SFEs, which is again consistent with the fact that noble metals have narrow bands compared to others (Fig. 4 and Figs. S7, S8 in the SM [79]), resulting in low SFEs.

Although some features have high correlation coefficients, a multivariable linear regression fails to accurately predict the target variables. Thus, we use other regression methods such as deep neural network (DNN), support vector regression (SVR), Gaussian process regression (GPR), and random forest. We split the data set for training and testing (80:20). The latter is used to test the trained model and compute the test error. The mean absolute error between the actual and predicted values gives the loss. We select the model that exhibits the highest coefficient of determination for total average  $R^2$  for the test set and the highest total  $R^2$  for the training set as the optimal one for each approach. The following discussion covers DNN and random forest, while SVR and GPR are given in Sec. II and Fig. S9 in the SM [79].

### 3. Deep neural network

DNNs can capture highly nonlinear relationships and complex patterns because of their highly flexible and expressive interconnected architecture [83]. We evaluate the performance of different activation functions, such as rectified linear unit (ReLU), leaky ReLU, and parametric ReLU (PReLU). PReLU demonstrates superior overall performance, achieving the highest accuracy among the tested activation functions with a test  $R^2$  of 0.995 for  $\gamma_{\text{ISF}}$  prediction, compared to leaky ReLU (0.993) and traditional ReLU (0.988). The neural network with PReLU activation showcases enhanced resistance to sample bias because of its adaptive nature to effectively modulate activation for negative inputs and minimize outliers' impact, while promoting superior generalization for a more reliable and stable predictive model than leaky ReLU and ReLU counterparts. Figures 6(a), 6(c), and 6(e) show the predicted vs actual values for the best models of DNN, which we train with 5–7 dense layers with a learning rate of  $10^{-3}$  with around 200–500 epochs for iterations. We evaluate the model's performance based on the test error and the change in loss with the iterations. Convergence with the number of iterations is shown in Fig. S10 in the SM [79]. The test  $R^2$  values of  $G$ ,  $\gamma_{\text{ISF}}$ , and  $\gamma_{\text{ESF}}$  are 0.973, 0.995, and 0.993, respectively. The mean absolute errors (MAEs) of  $G$ ,  $\gamma_{\text{ISF}}$ , and  $\gamma_{\text{ESF}}$  are 2.69 GPa, 3.24 mJ/m<sup>2</sup>, and 2.65 mJ/m<sup>2</sup>, respectively.

### 4. Random forest

While the DNN exhibited impressive accuracy in predicting, it is not possible to understand how  $\gamma_{\text{ISF}}$ ,  $\gamma_{\text{ESF}}$ , and  $G$  depend on the feature variables. Our next objective is to predict the expression for  $\gamma_{\text{ISF}}$ ,  $\gamma_{\text{ESF}}$ , and  $G$  in terms of the feature variables. For this purpose, one must perform high-order polynomial regression, such as quadratic regression. This method expands the sample space from the initial five parameters ( $\varepsilon_d$ ,  $W_d$ ,  $z_d$ ,  $r_0$ , and  $z_s$ ) to 20 parameters by incorporating

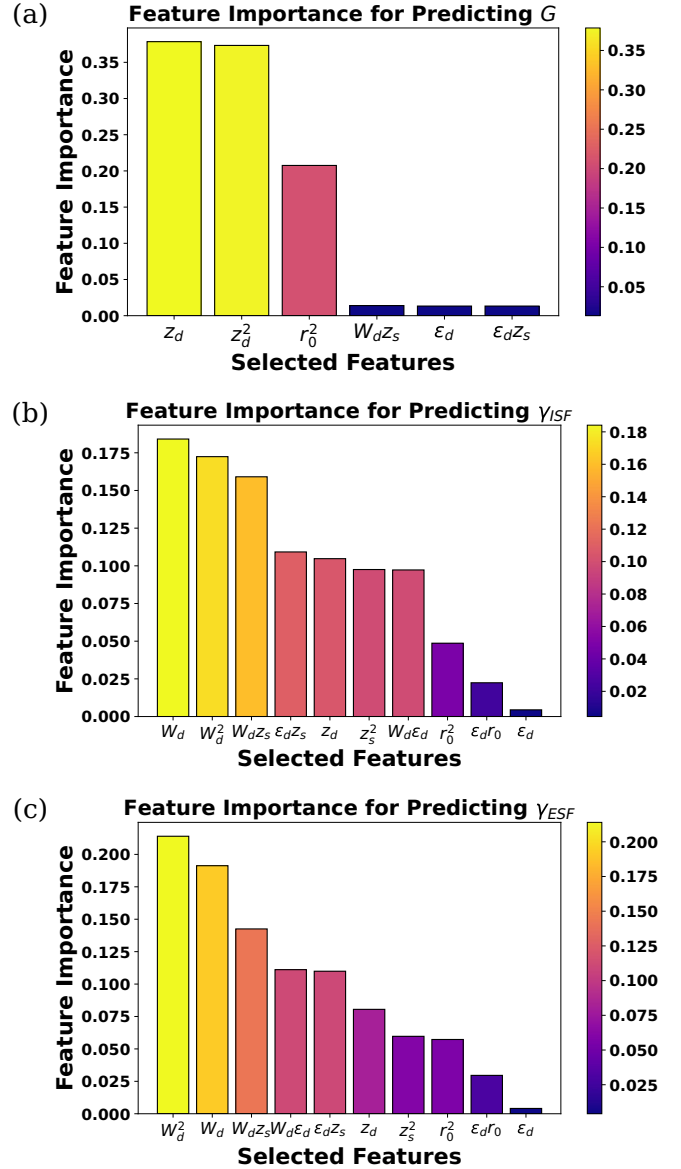


FIG. 7. Feature importance plot for  $G$ ,  $\gamma_{\text{ISF}}$ , and  $\gamma_{\text{ESF}}$ .

quadratic combinations. However, employing this approach may introduce redundant parameters, potentially leading to overfitting.

A strategy to mitigate overfitting is to utilize a random forest regressor, incorporating the quadratic terms. The advantage of employing random forest lies in its ability to perform regression and simultaneously provide insights into the minimum number of terms essential for optimal prediction without the issue of overfitting by performing a search using its randomly ensembled decision trees. This process is called feature importance analysis. Details of feature importance analysis using random forest are given in Sec. III in the SM [79]. After feature importance analysis, we select only six terms for shear modulus prediction and 10 terms for SFE prediction (Fig. 7). Finally, we do a multivariable linear regression with the selected features to obtain the following expressions, which can

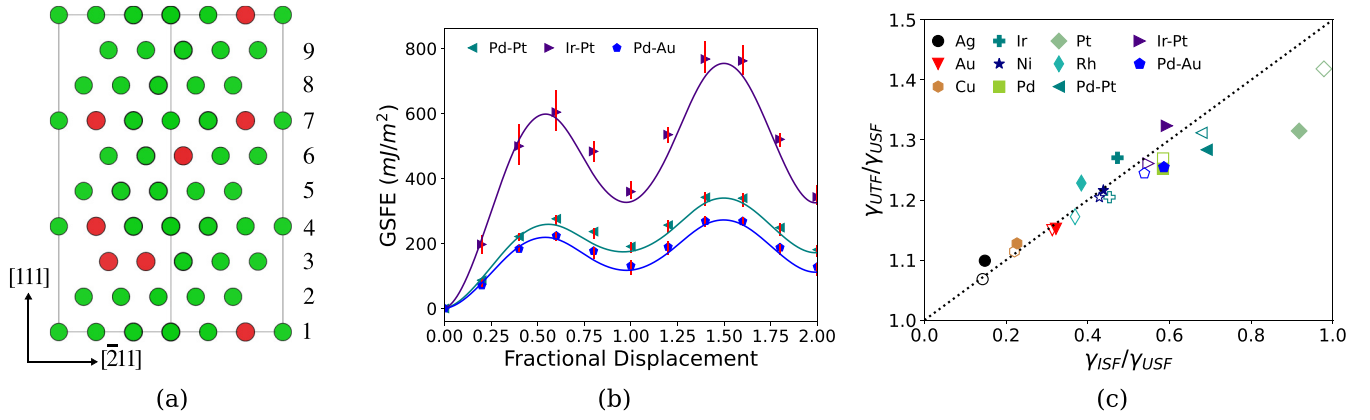


FIG. 8. (a) Supercell for GSFE calculation of alloys; numbers adjacent to the atomic planes represent the layer number. (b) GSFE curves for  $\text{Pd}_{0.75}\text{Pt}_{0.25}$ ,  $\text{Ir}_{0.75}\text{Pt}_{0.25}$ , and  $\text{Pd}_{0.75}\text{Au}_{0.25}$  alloys. The symbols are from DFT calculations, while the curves are generated from Eq. (2), using  $\gamma_{ISF}$ ,  $\gamma_{ESF}$ , and  $G$  values predicted via ML. (c)  $\gamma_{UTF}/\gamma_{USF}$  scales linearly with  $\gamma_{ISF}/\gamma_{USF}$ , as shown by the dotted line. Comparison of actual values from DFT calculations (solid symbols) and predicted values (open symbols).

be directly used for prediction:

$$G = 51.07z_d^2 - 63.21r_0^2 + 25.82\varepsilon_d - 876.15z_d + 33.80W_dz_s - 60.14\varepsilon_dz_s + 3877.91, \quad (9)$$

$$\gamma_{ISF} = -22.66W_d^2 - 579.36z_s^2 - 522.06r_0^2 - 220.46\varepsilon_d + 27.77z_d + 64.57W_d + 18.51W_d\varepsilon_d + 278.81W_dz_s - 49.31\varepsilon_dz_s + 74.77\varepsilon_d r_0 + 996.58, \quad (10)$$

$$\gamma_{ESF} = -21.29W_d^2 - 730.97z_s^2 - 453.58r_0^2 - 178.69\varepsilon_d + 31.77z_d + 78.59W_d + 16.30W_d\varepsilon_d + 249.45W_dz_s + 0.80\varepsilon_dz_s + 41.06\varepsilon_d r_0 + 781.64. \quad (11)$$

Note that before applying the feature importance selection analysis, the mean absolute error obtained by including all 20 terms are 6.38 GPa, 9.28 mJ/m², and 7.62 mJ/m² for  $G$ ,  $\gamma_{ISF}$ , and  $\gamma_{ESF}$  [insets of Figs. 6(b), 6(d), and 6(f)], which reduces to 3.99 GPa, 7.03 mJ/m², and 6.44 mJ/m² [Figs. 6(b), 6(d), and 6(f)], respectively. The test  $R^2$  values of  $G$ ,  $\gamma_{ISF}$ , and  $\gamma_{ESF}$  also improve from 0.928, 0.963, and 0.973 (with all 20 features) to 0.983, 0.987, and 0.989 (with selected features), respectively. The improvement can be attributed to keeping only essential features, thus reducing the problem of overfitting.

Figure 7 illustrates all the selected features that are utilized in predicting the formula [Eqs. (9)–(11)] in descending order in terms of their importance. Two features are dominant for shear modulus  $G$ : linear and quadratic terms of the number of  $d$  electrons ( $z_d$ ), followed by  $r_0^2$ . Stacking fault energies  $\gamma_{ISF}$  and  $\gamma_{ESF}$  depend on multiple features, the linear and quadratic term of  $d$ -band width ( $W_d$ ) being the most important among them. The list also contains some cross terms such as  $W_d\varepsilon_d$ ,  $W_dz_s$ ,  $\varepsilon_dz_s$  with non-negligible weight, highlighting the highly nonlinear nature of the problem, which requires a combined approach involving state-of-the-art *ab initio* calculations and machine learning methods for complete understanding.

#### D. GSFE curve prediction

So far, we have focused on training ML models for predicting  $\gamma_{ISF}$ ,  $\gamma_{ESF}$ , and  $G$ . Finally, we take up the most challenging task of predicting the entire GSFE. Conventionally, one should calculate the GSFE curves for several alloys using DFT and use them to train ML models. However, calculating the GSFE curves for alloys is computationally very expensive. Instead, we use the predicted  $G$ ,  $\gamma_{ISF}$ , and  $\gamma_{ESF}$  values from the previous section and construct the GSFE curves using Eq. (2). For a binary alloy, we use the rule of mixture to get the value of  $c$  [listed after Eq. (2)], which is the weighted average of the pure element's values. The following discussion shows that our method makes GSFE prediction 80x faster for alloys.

Figure 8 compares the predicted GSFE curves with actual DFT values, illustrated for binary Pd-Pt, Ir-Pt, and Pd-Au alloys. We use the same technique as described earlier (Fig. 2), but with a nine-times-larger supercell, having cell vectors  $\frac{3}{2}[\bar{1}10]$ ,  $\frac{3}{2}[\bar{1}01]$ ,  $[111]$ . Such a supercell contains 81 atoms, nine each in nine different layers [Fig. 8(a)]. We generate SQS to describe the random arrangement of constituent atoms in a binary alloy and use a  $k$ -point mesh of  $9 \times 9 \times 3$ . Because of the randomness, each layer has a different composition [Fig. 8(a)], and the GSFE curve depends on the specific choice of layers during the deformation. For example, we start by fixing layer 1 and displacing layers 2 to 9, followed by fixing layers 1 and 2, and displacing layers 3 to 9, etc., as shown in Fig. 8(a). Thus, we have to repeat the calculation eight times, and the average value yields one single DFT data point on a GSFE curve [Fig. 8(b)]. The error bars show the lowest and highest among the eight calculated DFT values. Since there are 10 data points on a GSFE curve, we need to perform 80 calculations to directly get the entire GSFE curve from DFT.

Considering the large number of atoms in the supercell, predicting GSFE directly from DFT is computationally expensive for alloys. As an alternative, the proposed ML approach requires only one DFT calculation to get the DOS and compute relevant parameters such as  $\varepsilon_d$ ,  $W_d$ ,  $z_d$ ,  $z_s$ , and  $r_0$ . Using these parameters, one can predict  $\gamma_{ISF}$ ,  $\gamma_{ESF}$ , and  $G$  using the ML model and finally predict the GSFE curve using Eq. (2).



Figure 8(b) illustrates that the ML-predicted GSFE curves are in good agreement with the actual DFT points (based on 80 DFT calculations). As shown in Fig. 8(c),  $\gamma_{\text{UTF}}/\gamma_{\text{USF}}$  scales linearly with  $\gamma_{\text{ISF}}/\gamma_{\text{USF}}$ . The predicted values agree reasonably well with the DFT results.

#### IV. CONCLUSIONS

In conclusion, we have proposed a combined *ab initio* and ML-based model that can accelerate the computational prediction of GSFE curves for alloys by a factor of 80. The training dataset is generated using DFT calculations to find the SFE values of 106 metals and alloys using the ANNNI model. The features used for training the ML algorithms come from the physics-based Friedel model. The features are obtained from the electronic DOS, calculated using DFT. Other than accelerating the process of GSFE calculation, the present work also highlights a deep connection between the physics of *d* electrons and the deformation behavior of transition metals and alloys. Our study reveals a highly nonlinear dependence

of shear modulus and stacking fault energies on the electronic features, which requires a combined approach involving state-of-the-art *ab initio* calculations and machine learning methods for complete understanding. In terms of practical applications, the present model can accelerate alloy design with targeted mechanical behavior by providing a fast method of screening materials in terms of stacking fault energies. We plan to further extend the model for medium and high entropy alloys in the future.

#### ACKNOWLEDGMENTS

We acknowledge the National Super Computing Mission (NSM) for providing computing resources of “PARAM Sanganak” at IIT Kanpur, which is implemented by CDAC and supported by the Ministry of Electronics and Information Technology (MeitY) and Department of Science and Technology (DST), Government of India. We also thank ICME National Hub, IIT Kanpur and CC, IIT Kanpur for providing the HPC facility.

- 
- [1] D. Molnár, X. Sun, S. Lu, W. Li, G. Engberg, and L. Vitos, Effect of temperature on the stacking fault energy and deformation behaviour in 316L austenitic stainless steel, *Mater. Sci. Eng. A* **759**, 490 (2019).
- [2] X. Zhang, B. Grabowski, F. Körmann, A. V. Ruban, Y. Gong, R. C. Reed, T. Hickel, and J. Neugebauer, Temperature dependence of the stacking-fault Gibbs energy for Al, Cu, and Ni, *Phys. Rev. B* **98**, 224106 (2018).
- [3] P. Andric, B. Yin, and W. Curtin, Stress-dependence of generalized stacking fault energies, *J. Mech. Phys. Solids* **122**, 262 (2019).
- [4] A. Linda, P. K. Tripathi, S. Nagar, and S. Bhowmick, Effect of pressure on stacking fault energy and deformation behavior of face-centered-cubic metals, *Materialia* **26**, 101598 (2022).
- [5] Q. Shao, L. Liu, T. Fan, D. Yuan, and J. Chen, Effects of solute concentration on the stacking fault energy in copper alloys at finite temperatures, *J. Alloys Compd.* **726**, 601 (2017).
- [6] J. Kumar, A. Linda, M. Sadhasivam, K. Pradeep, N. Gurao, and K. Biswas, The effect of Si addition on the structure and mechanical properties of equiatomic CoCrFeMnNi high entropy alloy by experiment and simulation, *Materialia* **27**, 101707 (2023).
- [7] Y. Zhang, J. Guo, J. Chen, C. Wu, K. S. Kormout, P. Ghosh, and Z. Zhang, On the stacking fault energy related deformation mechanism of nanocrystalline Cu and Cu alloys: A first-principles and TEM study, *J. Alloys Compd.* **776**, 807 (2019).
- [8] S. Zhao, G. M. Stocks, and Y. Zhang, Stacking fault energies of face-centered-cubic concentrated solid solution alloys, *Acta Mater.* **134**, 334 (2017).
- [9] L. Li, Z. Zhang, P. Zhang, and Z. Zhang, A review on the fatigue cracking of twin boundaries: Crystallographic orientation and stacking fault energy, *Prog. Mater. Sci.* **131**, 101011 (2023).
- [10] R. Su, D. Neffati, Y. Zhang, J. Cho, J. Li, H. Wang, Y. Kulkarni, and X. Zhang, The influence of stacking faults on mechanical behavior of advanced materials, *Mater. Sci. Eng. A* **803**, 140696 (2021).
- [11] X. An, S. Wu, Z. Wang, and Z. Zhang, Significance of stacking fault energy in bulk nanostructured materials: Insights from Cu and its binary alloys as model systems, *Prog. Mater. Sci.* **101**, 1 (2019).
- [12] C. Tian, G. Han, C. Cui, and X. Sun, Effects of stacking fault energy on the creep behaviors of Ni-base superalloy, *Mater. Des.* **64**, 316 (2014).
- [13] P. Delavignette and S. Amelinckx, Dislocation patterns in graphite, *J. Nucl. Mater.* **5**, 17 (1962).
- [14] K. V. Werner, F. Niessen, M. Villa, and M. A. J. Somers, Experimental validation of negative stacking fault energies in metastable face-centered-cubic materials, *Appl. Phys. Lett.* **119**, 141902 (2021).
- [15] D. Rafaja, C. Krubetschek, C. Ullrich, and S. Martin, Stacking fault energy in austenitic steels determined by using *in situ* x-ray diffraction during bending, *J. Appl. Crystallogr.* **47**, 936 (2014).
- [16] T. Byun, On the stress dependence of partial dislocation separation and deformation microstructure in austenitic stainless steels, *Acta Mater.* **51**, 3063 (2003).
- [17] Y. Su, S. Xu, and I. J. Beyerlein, Density functional theory calculations of generalized stacking fault energy surfaces for eight face-centered-cubic transition metals, *J. Appl. Phys.* **126**, 105112 (2019).
- [18] A. Hunter, R. F. Zhang, and I. J. Beyerlein, The core structure of dislocations and their relationship to the material  $\gamma$ -surface, *J. Appl. Phys.* **115**, 134314 (2014).
- [19] Q.-M. Hu and R. Yang, Basal-plane stacking fault energy of hexagonal close-packed metals based on the Ising model, *Acta Mater.* **61**, 1136 (2013).
- [20] X.-Z. Wu, R. Wang, S.-F. Wang, and Q.-Y. Wei, *Ab initio* calculations of generalized-stacking-fault energy surfaces and surface energies for fcc metals, *Appl. Surf. Sci.* **256**, 6345 (2010).

- [21] A. Jarlöv, W. Ji, Z. Zhu, Y. Tian, R. Babicheva, R. An, H. L. Seet, M. L. S. Nai, and K. Zhou, Molecular dynamics study on the strengthening mechanisms of Cr-Fe-Co-Ni high-entropy alloys based on the generalized stacking fault energy, *J. Alloys Compd.* **905**, 164137 (2022).
- [22] B. Joós, Q. Ren, and M. S. Duesbery, Peierls-Nabarro model of dislocations in silicon with generalized stacking-fault restoring forces, *Phys. Rev. B* **50**, 5890 (1994).
- [23] J. Hartford, B. von Sydow, G. Wahnström, and B. I. Lundqvist, Peierls barriers and stresses for edge dislocations in Pd and Al calculated from first principles, *Phys. Rev. B* **58**, 2487 (1998).
- [24] S. L. Shang, W. Y. Wang, Y. Wang, Y. Du, J. X. Zhang, A. D. Patel, and Z. K. Liu, Temperature-dependent ideal strength and stacking fault energy of fcc Ni: A first-principles study of shear deformation, *J. Phys.: Condens. Matter* **24**, 155402 (2012).
- [25] S. L. Shang, C. L. Zacherl, H. Z. Fang, Y. Wang, Y. Du, and Z. K. Liu, Effects of alloying element and temperature on the stacking fault energies of dilute Ni-base superalloys, *J. Phys.: Condens. Matter* **24**, 505403 (2012).
- [26] H. El Kadiri, J. Kapil, A. L. Oppedal, L. G. Hector, Jr., S. R. Agnew, M. Cherkaoui, and S. C. Vogel, The effect of twin-twin interactions on the nucleation and propagation of 1012 twinning in magnesium, *Acta Mater.* **61**, 3549 (2013).
- [27] A. Linda, M. F. Akhtar, and S. Bhowmick, Deformation in metals: Insights from *ab initio* calculations, in *Proceedings of the International Conference on Metallurgical Engineering and Centenary Celebration*, edited by S. Patra, S. Sinha, G. S. Mahobia, and D. Kamble (Springer Nature Singapore, Singapore, 2024), pp. 83–92.
- [28] Y. Kamimura, K. Edagawa, A. Iskandarov, M. Osawa, Y. Umeno, and S. Takeuchi, Peierls stresses estimated via the Peierls-Nabarro model using *ab initio*  $\gamma$  surface and their comparison with experiments, *Acta Mater.* **148**, 355 (2018).
- [29] S. Xu, J. R. Mianroodi, A. Hunter, B. Svendsen, and I. J. Beyerlein, Comparative modeling of the disregistry and Peierls stress for dissociated edge and screw dislocations in Al, *Intl. J. Plast.* **129**, 102689 (2020).
- [30] T. Ma, H. Kim, N. Mathew, D. J. Luscher, L. Cao, and A. Hunter, Dislocation transmission across  $\sigma$ 3112 incoherent twin boundary: A combined atomistic and phase-field study, *Acta Mater.* **223**, 117447 (2022).
- [31] S. Schönecker, W. Li, L. Vitos, and X. Li, Effect of strain on generalized stacking fault energies and plastic deformation modes in fcc-hcp polymorphic high-entropy alloys: A first-principles investigation, *Phys. Rev. Mater.* **5**, 075004 (2021).
- [32] L. Zhu and Z. Wu, Effects of short range ordering on the generalized stacking fault energy and deformation mechanisms in fcc multiprincipal element alloys, *Acta Mater.* **259**, 119230 (2023).
- [33] C. Yang, B. Zhang, L. Fu, Z. Wang, J. Teng, R. Shao, Z. Wu, X. Chang, J. Ding, L. Wang, and X. Han, Chemical inhomogeneity-induced profuse nanotwinning and phase transformation in AuCu nanowires, *Nat. Commun.* **14**, 5705 (2023).
- [34] D. Wen, B. Kong, S. Wang, L. Liu, Q. Song, and Z. Yin, Mechanism of stress- and thermal-induced fct  $\rightarrow$  hcp  $\rightarrow$  fcc crystal structure change in a TiAl-based alloy compressed at elevated temperature, *Mater. Sci. Eng. A* **840**, 143011 (2022).
- [35] Z. Pei, B. Dutta, F. Körmann, and M. Chen, Hidden effects of negative stacking fault energies in complex concentrated alloys, *Phys. Rev. Lett.* **126**, 255502 (2021).
- [36] K. V. Werner, F. Niessen, W. Li, S. Lu, L. Vitos, M. Villa, and M. A. Somers, Reconciling experimental and theoretical stacking fault energies in face-centered-cubic materials with the experimental twinning stress, *Materialia* **27**, 101708 (2023).
- [37] D. You, O. K. Celebi, A. S. K. Mohammed, and H. Sehitoglu, Negative stacking fault energy in fcc materials-Its implications, *Intl. J. Plast.* **170**, 103770 (2023).
- [38] S. Wei and C. C. Tasan, Deformation faulting in a metastable CoCrNiW complex concentrated alloy: A case of negative intrinsic stacking fault energy? *Acta Mater.* **200**, 992 (2020).
- [39] M. Shih, J. Miao, M. Mills, and M. Ghazisaeidi, Stacking fault energy in concentrated alloys, *Nat. Commun.* **12**, 3590 (2021).
- [40] M. Walter, L. Mujica Roncery, S. Weber, L. Leich, and W. Theisen, Xrd measurement of stacking fault energy of Cr-Ni austenitic steels: influence of temperature and alloying elements, *J. Mater. Sci.* **55**, 13424 (2020).
- [41] A. Chandan, S. Tripathy, B. Sen, M. Ghosh, and S. Ghosh Chowdhury, Temperature dependent deformation behavior and stacking fault energy of Fe<sub>40</sub>Mn<sub>40</sub>Co<sub>10</sub>Cr<sub>10</sub> alloy, *Scr. Mater.* **199**, 113891 (2021).
- [42] X. Sun, S. Lu, R. Xie, X. An, W. Li, T. Zhang, C. Liang, X. Ding, Y. Wang, H. Zhang, and L. Vitos, Can experiment determine the stacking fault energy of metastable alloys? *Mater. Des.* **199**, 109396 (2021).
- [43] H. Hu, M. Zhao, X. Wu, Z. Jia, R. Wang, W. Li, and Q. Liu, The structural stability, mechanical properties and stacking fault energy of Al<sub>3</sub>Zr precipitates in Al-Cu-Zr alloys: Hrtem observations and first-principles calculations, *J. Alloys Compd.* **681**, 96 (2016).
- [44] S. Shi, L. Zhu, H. Zhang, Z. Sun, and R. Ahuja, Mapping the relationship among composition, stacking fault energy and ductility in Nb alloys: A first-principles study, *Acta Mater.* **144**, 853 (2018).
- [45] H. Stange, S. Brunken, H. Hempel, H. Rodriguez-Alvarez, N. Schäfer, D. Greiner, A. Scheu, J. Lauche, C. A. Kaufmann, T. Unold, D. Abou-Ras, and R. Mainz, Effect of Na presence during CuInSe<sub>2</sub> growth on stacking fault annihilation and electronic properties, *Appl. Phys. Lett.* **107**, 152103 (2015).
- [46] W. Y. Wang, S. L. Shang, Y. Wang, Z.-G. Mei, K. A. Darling, L. J. Kecskes, S. N. Mathaudhu, X. D. Hui, and Z.-K. Liu, Effects of alloying elements on stacking fault energies and electronic structures of binary Mg alloys: A first-principles study, *Mater. Res. Lett.* **2**, 29 (2014).
- [47] X. Li, S. Schönecker, L. Vitos, and X. Li, Generalized stacking faults energies of face-centered cubic high-entropy alloys: A first-principles study, *Intermetallics* **145**, 107556 (2022).
- [48] Y. Qi and R. K. Mishra, *Ab initio* study of the effect of solute atoms on the stacking fault energy in aluminum, *Phys. Rev. B* **75**, 224105 (2007).
- [49] A. R. Natarajan and A. Van der Ven, Linking electronic structure calculations to generalized stacking fault energies in multicomponent alloys, *npj Comput. Mater.* **6**, 80 (2020).
- [50] I. Harris, I. Dillamore, R. Smallman, and B. Beeston, The influence of *d*-band structure on stacking-fault energy, *Philos. Mag.* **14**, 325 (1966).
- [51] A. Datta, U. Waghmare, and U. Ramamurty, Structure and stacking faults in layered Mg-Zn-Y alloys: A first-principles study, *Acta Mater.* **56**, 2531 (2008).

- [52] K. Kumar, R. Sankarasubramanian, and U. V. Waghmare, Influence of dilute solute substitutions in Ni on its generalized stacking fault energies and ductility, *Comput. Mater. Sci.* **150**, 424 (2018).
- [53] Y. Shen, H. Wang, and Q. An, Modified generalized stacking fault energy surface of II-VI ionic crystals from excess electrons and holes, *ACS Appl. Electron. Mater.* **2**, 56 (2020).
- [54] Z. Li, J. R. Kermode, and A. De Vita, Molecular dynamics with on-the-fly machine learning of quantum-mechanical forces, *Phys. Rev. Lett.* **114**, 096405 (2015).
- [55] O. Ahmad, N. Kumar, R. Mukherjee, and S. Bhowmick, Accelerating microstructure modeling via machine learning: A method combining autoencoder and convlstm, *Phys. Rev. Mater.* **7**, 083802 (2023).
- [56] K. T. Schütt, H. Glawe, F. Brockherde, A. Sanna, K. R. Müller, and E. K. U. Gross, How to represent crystal structures for machine learning: Towards fast prediction of electronic properties, *Phys. Rev. B* **89**, 205118 (2014).
- [57] H. Zhang, H. Fu, X. He, C. Wang, L. Jiang, L.-Q. Chen, and J. Xie, Dramatically enhanced combination of ultimate tensile strength and electric conductivity of alloys via machine learning screening, *Acta Mater.* **200**, 803 (2020).
- [58] X. Liu, X. Li, Q. He, D. Liang, Z. Zhou, J. Ma, Y. Yang, and J. Shen, Machine learning-based glass formation prediction in multicomponent alloys, *Acta Mater.* **201**, 182 (2020).
- [59] Y. V. Krishna, U. K. Jaiswal, and R. M. R., Machine learning approach to predict new multiphase high entropy alloys, *Scr. Mater.* **197**, 113804 (2021).
- [60] V. Revi, S. Kasodariya, A. Talapatra, G. Pilania, and A. Alankar, Machine learning elastic constants of multi-component alloys, *Comput. Mater. Sci.* **198**, 110671 (2021).
- [61] X. Chong, S.-L. Shang, A. M. Krajewski, J. D. Shimanek, W. Du, Y. Wang, J. Feng, D. Shin, A. M. Beese, and Z.-K. Liu, Correlation analysis of materials properties by machine learning: illustrated with stacking fault energy from first-principles calculations in dilute fcc-based alloys, *J. Phys.: Condens. Matter* **33**, 295702 (2021).
- [62] S. Mahato, N. P. Gurao, and K. Biswas, Accelerated prediction of stacking fault energy in fcc medium entropy alloys using multilayer perceptron neural networks: Correlation and feature analysis, *Model. Simul. Mater. Sci. Eng.* **32**, 035021 (2024).
- [63] X. Liu, Y. Zhu, C. Wang, K. Han, L. Zhao, S. Liang, M. Huang, and Z. Li, A statistics-based study and machine-learning of stacking fault energies in HeAs, *J. Alloys Compd.* **966**, 171547 (2023).
- [64] Y.-J. Hu, A. Sundar, S. Ogata, and L. Qi, Screening of generalized stacking fault energies, surface energies and intrinsic ductile potency of refractory multicomponent alloys, *Acta Mater.* **210**, 116800 (2021).
- [65] M. Wang, H. Yu, Y. Chen, and M. Huang, Machine learning assisted screening of non-rare-earth elements for Mg alloys with low stacking fault energy, *Comput. Mater. Sci.* **196**, 110544 (2021).
- [66] T. Z. Khan, T. Kirk, G. Vazquez, P. Singh, A. Smirnov, D. D. Johnson, K. Youssef, and R. Arróyave, Towards stacking fault energy engineering in fcc high entropy alloys, *Acta Mater.* **224**, 117472 (2022).
- [67] G. Arora, A. Manzoor, and D. S. Aidhy, Charge-density based evaluation and prediction of stacking fault energies in Ni alloys from DFT and machine learning, *J. Appl. Phys.* **132**, 225104 (2022).
- [68] G. Arora, S. Kamrava, P. Tahmasebi, and D. S. Aidhy, Charge-density based convolutional neural networks for stacking fault energy prediction in concentrated alloys, *Materialia* **26**, 101620 (2022).
- [69] G. Kresse and D. Joubert, From ultrasoft pseudopotentials to the projector augmented-wave method, *Phys. Rev. B* **59**, 1758 (1999).
- [70] G. Kresse and J. Furthmüller, Efficient iterative schemes for *ab initio* total energy calculations using a plane-wave basis set, *Phys. Rev. B* **54**, 11169 (1996).
- [71] J. P. Perdew, K. Burke, and M. Ernzerhof, Generalized gradient approximation made simple, *Phys. Rev. Lett.* **77**, 3865 (1996).
- [72] I. L. Dillamore and R. E. Smallman, The stacking-fault energy of fcc metals, *Philos. Mag.* **12**, 191 (1965).
- [73] P. C. J. Gallagher, The influence of alloying, temperature, and related effects on the stacking fault energy, *Metal. Trans.* **1**, 2429 (1970).
- [74] J. P. Hirth, J. Lothe, and T. Mura, Theory of dislocations, *J. Appl. Mech.* **50**, 476 (1983).
- [75] A. Buch, *Short Handbook of Metal Elements Properties and Elastic Properties of Pure Metals*, 3rd ed. (Krzyzstof Biesaga, Warsaw, 2005).
- [76] S. Kibey, J. B. Liu, D. D. Johnson, and H. Sehitoglu, Energy pathways and directionality in deformation twinning, *Appl. Phys. Lett.* **91**, 181916 (2007).
- [77] Y. Le Page and P. Saxe, Symmetry-general least-squares extraction of elastic coefficients from *ab initio* total energy calculations, *Phys. Rev. B* **63**, 174103 (2001).
- [78] V. Wang, N. Xu, J.-C. Liu, G. Tang, and W.-T. Geng, Vaspkit: A user-friendly interface facilitating high-throughput computing and analysis using VASP code, *Comput. Phys. Commun.* **267**, 108033 (2021).
- [79] See Supplemental Material at <http://link.aps.org/supplemental/10.1103/PhysRevB.109.214102> for technical details of shear modulus calculation, materials parameters calculated from density functional theory, Gaussian process regression, support vector regression, and feature importance analysis.
- [80] M. Ruffino, G. C. G. Skinner, E. I. Andritsos, and A. T. Paxton, Ising-like models for stacking faults in a free electron metal, *Proc. R. Soc. A* **476**, 20200319 (2020).
- [81] W. A. Harrison, *Electronic Structure and the Properties of Solids: The Physics of the Chemical Bond* (Dover Publications, New York, 2012).
- [82] A. van de Walle, P. Tiwary, M. de Jong, D. Olmsted, M. Asta, A. Dick, D. Shin, Y. Wang, L.-Q. Chen, and Z.-K. Liu, Efficient stochastic generation of special quasirandom structures, *Calphad* **42**, 13 (2013).
- [83] J. Schmidhuber, Deep learning in neural networks: An overview, *Neural Networks* **61**, 85 (2015).